Taylor & Francis
Taylor & Francis Group

Computer Methods in Biomechanics and Biomedical Engineering

ISSN: 1025-5842 (Print) 1476-8259 (Online) Journal homepage: https://www.tandfonline.com/loi/gcmb20

Finite element studies of the mechanical behaviour of the diaphragm in normal and pathological cases

M. P.M. Pato , N. J.G. Santos , P. Areias , E. B. Pires , M. de Carvalho , S. Pinto & D. S. Lopes

To cite this article: M. P.M. Pato , N. J.G. Santos , P. Areias , E. B. Pires , M. de Carvalho , S. Pinto & D. S. Lopes (2011) Finite element studies of the mechanical behaviour of the diaphragm in normal and pathological cases, Computer Methods in Biomechanics and Biomedical Engineering, 14:06, 505-513, DOI: 10.1080/10255842.2010.483683

To link to this article: https://doi.org/10.1080/10255842.2010.483683

Computer Methods in Biomechanics and Biomedical Engineering
Vol. 14, No. 6, June 2011, 505–513

Taylor & Francis
Taylor & Francis Group

Finite element studies of the mechanical behaviour of the diaphragm in normal and pathological cases

M.P.M. Pato[a,b]*, N.J.G. Santos[b], P. Areias[b,c], E.B. Pires[b], M. de Carvalho[d], S. Pinto[d] and D.S. Lopes[e]

[a]*Instituto Superior de Engenharia de Lisboa, Rua Conselheiro Emídio Navarro, Lisbon, Portugal*
[b]*ICIST/Instituto Superior Técnico, Technical University of Lisbon, Av. Rovisco Pais, 1049-001 Lisbon, Portugal;* [c]*Universidade de Évora, Largo dos Colegiais, 2, 7004-516 Évora, Portugal;* [d]*Neuromuscular Unit, Instituto de Medicina Molecular, University of Lisbon, Av. Professor Egas Moniz, 1649-028 Lisbon, Portugal;* [e]*IDMEC/Instituto Superior Técnico, Technical University of Lisbon, Av. Rovisco Pais, 1049-001 Lisbon, Portugal*

(*Received 2 January 2010; final version received 5 April 2010*)

The diaphragm is a muscular membrane separating the abdominal and thoracic cavities, and its motion is directly linked to respiration. In this study, using data from a 59-year-old female cadaver obtained from the Visible Human Project, the diaphragm is reconstructed and, from the corresponding solid object, a shell finite element mesh is generated and used in several analyses performed with the ABAQUS 6.7 software. These analyses consider the direction of the muscle fibres and the incompressibility of the tissue. The constitutive model for the isotropic strain energy as well as the passive and active strain energy stored in the fibres is adapted from Humphrey's model for cardiac muscles. Furthermore, numerical results for the diaphragmatic floor under pressure and active contraction in normal and pathological cases are presented.

Keywords: diaphragm; active behaviour; amyotrophic lateral sclerosis; right phrenic nerve lesion; shell finite elements

1. Introduction

The diaphragm is the major muscle of respiration and separates the thoracic and abdominal cavities. It is a thin and flat modified half-dome of musculofibrous tissue that originates from the lower six ribs bilaterally, the posterior xiphoid process as well as the external and internal arcuate ligaments. A number of different structures cross the diaphragm, but three distinct apertures allow the passage of the aorta, oesophagus and vena cava. The aortic aperture is the lowest and most posterior of the openings, lying at the level of the 12th thoracic vertebra. The oesophageal aperture is surrounded by diaphragmatic muscle and lies at the level of the tenth thoracic vertebra. The vena cava aperture is the highest of the three openings and lies at the level of the disc space between the eighth and ninth thoracic vertebrae (Harrison 2005).

The respiratory muscles are skeletal muscles. The inspiratory muscles include the diaphragm, external intercostal, parasternal, sternomastoid and scalene muscles. The expiratory muscles include the internal intercostal, rectus abdominis, external and internal oblique and transverse abdominis muscles. During inspiration, the diaphragm contracts, while expiration is generally a passive process (Ratnovsky et al. 2008).

The muscle fibres of the diaphragm radiate from the central tendon to either the three lumbar vertebral bodies (i.e. crural diaphragm) or to the inner surfaces of the lower six ribs (i.e. costal diaphragm). The costal fibres of the diaphragm are driven independently and form a two-sided muscle sheet. The tension within the diaphragmatic muscle fibres during contraction generates a caudal force on the central tendon that descends in order to expand the thoracic cavity along its craniocaudal axis. In addition, the costal diaphragm fibres apply a force on the lower six ribs, which lifts and rotates them outward (de Troyer et al. 1997).

The body relies on the diaphragm for normal respiratory function. Contraction of the diaphragm has the following functions: (1) decreasing intrapleural pressure, (2) expanding the rib cage through its region of apposition by generating positive intra-abdominal pressure and (3) expanding the rib cage using the abdomen as a fulcrum.

A respiratory dysfunction is observed when a decrease in the diaphragmatic function occurs. The body possesses inherent mechanisms of compensation for decreased diaphragmatic function, but none of the processes can successfully prevent respiratory compromise if the diaphragm excursion is diminished.

The diagnosis of the decreased function of diaphragm typically consists of observation of both neurological and anatomical processes. Neurologic problems of the diaphragm occur when a traumatic injury or disease process decreases or terminates the impulse of respiratory stimuli originating from the brainstem. Neurologic and other disorders decrease the integrity of the musculature of the diaphragm, thus decreasing its excursion. These problems ultimately result in the inability of the

*Corresponding author. Email: mpato@civil.ist.utl.pt

ISSN 1025-5842 print/ISSN 1476-8259 online

DOI: 10.1080/10255842.2010.483683
http://www.informaworld.com

diaphragm to provide adequate negative intra-thoracic pressure, thereby decreasing the amount of oxygen provided to the alveoli.

For instance, the amyotrophic lateral sclerosis (ALS) is a neurological disease that causes respiratory failure and death. This is a rapid progressive condition, which leads to severe weakness and disability, associated with a poor quality of life. When the diaphragm fails, the patients manifest respiratory symptoms and eventually lose the ability to breath without ventilatory support. The mean survival after the onset of the disease is 3–5 years. However, about 10% of the ALS patients survive for 10 years or more (de Mamede 2002).

There are other causes of diaphragm paralysis, namely, those derived from phrenic nerve injury. The central nervous system and the diaphragm are connected by the phrenic nerve. Each half of the diaphragm is innervated by the left and right phrenic nerves. When one of the phrenic nerves is injured as a consequence of a surgical intervention or an inflammatory process, the corresponding hemidiaphragm paralyses. Several studies have been performed to obtain the respiratory consequence encountered in the unilateral paralysis of the diaphragm. In one of these studies (Laroche et al. 1998), 11 patients experiencing unilateral diaphragm paralysis were monitored. Increase in breathlessness and decrease in exercise tolerance were reported, but the patients could breathe by themselves and the need of auxiliary ventilation was not referred.

In this work, a previously developed computational model (d'Aulignac et al. 2005; Martins et al. 2006, 2007) for the passive and active contraction of skeletal muscles is considered with the objective of studying the behaviour of the diaphragm during the respiratory cycle in normal and pathological cases. In the next section, a geometrical model of the diaphragm is presented. In Section 3, the constitutive equations are described. In Section 4, the computational model is applied to the reconstructed surface of the diaphragm and the corresponding numerical results are presented. Finally, in Section 5, some conclusions are drawn and future developments are listed.

2. Geometrical model

Owing to its anatomical complexity and dynamic mobility, the construction of a geometrical model of the diaphragm is a difficult task when relying on standard medical imaging. Here, data from the Visible Female Project (Ackerman 1998; Spitzer et al. 1996) are used to reconstruct the outer surface of the diaphragm. The images are real-colour cryosections containing a paramount of anatomical information. A total of 905 axial images of the thoracic and abdominal body segments, with $0.33 \times 0.33 \times 0.33\,\mathrm{mm}^3$ voxel dimensions and a colour

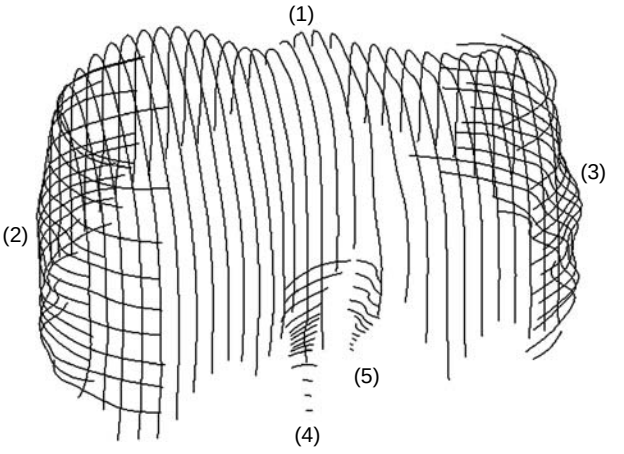

Figure 1. Five sets of curves identifying the diaphragm: (1) sagittal; (2) and (3) axial apposition region; (4) and (5) axial view of pillars inserted in the vertebral column.

resolution of 24 bits, are available in the Visible Human Project. The 3D reconstruction was performed as follows: (1) segmentation of axial and sagittal images, delimiting the outside border with cubic splines obtaining a contour network (Figure 1) and (2) interpolation of neighbouring curves with non-uniform rational basis spline (NURBS) surfaces. These steps were performed with the Rhinoceros® software (http://www.rhino3d.com). From the segmented images, five sets of curves were created: the sagittal curves represent almost the totality of the anterior, posterior and superior parts (set 1 in Figure 1); the two lateral sets of curves (sets 2 and 3 in Figure 1) form the more vertical part, called apposition region, while the other two axial sets of segments represent (sets 4 and 5 in Figure 1) the pillars of the diaphragm. The interpolated surfaces were discretised in triangular meshes. Mesh imperfections, e.g. holes and incoherent C^0 and C^1 continuity unification between sets, were corrected with the Blender software (http://www.blender.org/) (Figure 2)

Figure 2. Triangular surface of the diaphragm obtained with Blender.

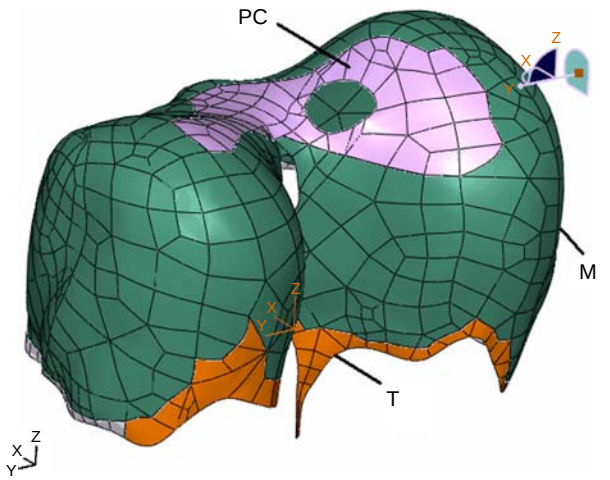

Figure 3. 3D solid object of the diaphragm obtained from ABAQUS: PC, phrenic centre; M, muscle; T, tendon.

(Lopes et al. 2008). This triangular surface provided a discrete representation of the geometric locus of the entire diaphragm floor.

Further modelling of the muscular and tendinous parts was performed with the ScanTo3D toolbox® (Figure 3), thus building a 3D solid model (NURBS patches). This object was finally imported to ABAQUS® 6.7 (see Santos 2009) to generate a finite element (FE) mesh. Manual segmentation and 3D model reconstruction were always performed under the supervision of skilled anatomists.

3. Mechanical model

The diaphragm is mainly formed by two types of tissues: tendon and muscle. Both the phrenic centre on the top and the tissue connected to the bones are composed of tendon. The remaining part of the diaphragm is formed by muscle. Accordingly, three main regions are created: the phrenic centre, the muscle and the tendon region in the inferior border of the diaphragm, shortly referred to as the inferior tendon (see Figure 3). These three regions are identified in the model by comparing it with the images provided in Netter (http://www.netterimages.com/image/atlas.htm) (see Santos 2009 for details).

The constitutive equation for 3D skeletal muscles adopted in the present work incorporates both passive and active behaviours. Following previous works (d'Aulignac et al. 2005; Martins et al. 2006, 2007), a modified form of the incompressible transversely isotropic hyperelastic model proposed by Humphrey and Yin (1987) for passive cardiac muscle has been considered.

The constitutive equation for the Cauchy stress is the sum of an incompressible term, an assumed embedding matrix term and a stress contribution term from the muscle fibres:

$$\sigma = \sigma_{\text{incomp}} + \sigma_{\text{matrix}} + \sigma_{\text{fibre}}. \tag{1}$$

The first contribution, in the case of perfect incompressibility, has the form:

$$\sigma_{\text{incomp}} = -p\mathbf{I}, \tag{2}$$

where p is the hydrostatic pressure and $\mathbf{I}$ the second-order identity tensor.

The matrix contribution is assumed to be hyperelastic and isotropic. This term has the same exponential form adopted by Humphrey and Yin (1987), but with material parameters obtained in some compression experiments with skeletal muscles available in the literature (Grieve and Armstrong 1988), which can be given by:

$$\sigma_{\text{matrix}} = 2bc \exp\left[b\left(I_1^{\text{C}} - 3\right)\right] \text{dev}[\mathbf{B}], \tag{3}$$

where I_1^{C} is the first invariant of $\mathbf{C}$, the right Cauchy–Green strain tensor, $\mathbf{B}$ is the left Cauchy–Green strain tensor and b and c are the constants. The deviatoric operator in the current configuration can be expressed by:

$$\text{dev}[\bullet] = (\bullet) - \frac{1}{3}\text{tr}(\bullet)\mathbf{I},$$

with $\bullet \in \text{Lin}$. The operator dev[•] is a projection linear transformation.

Much of the research on the contraction of skeletal muscles has focused on their 1D behaviour along the fibres. One of the most well known of the proposed models is Hill's muscle model (Hill 1938; Pandy et al. 1990; Fung 1993), shown in Figure 4.

The stress contribution of the muscle fibres has the form:

$$\sigma_{\text{fibre}} = \text{dev}[\lambda_{\text{f}} T \mathbf{n} \otimes \mathbf{n}], \tag{4}$$

where λ_{f} is the stretch ratio in the muscle fibres that have the direction of the unit vector $\mathbf{N}$ in the undeformed configuration. As incompressibility is assumed, λ_{f} is given by

$$\lambda_{\text{f}} = \sqrt{\mathbf{N}^T \mathbf{C} \mathbf{N}}.$$

The scalar T represents the nominal stress in the fibre and is the sum of the stresses T^{PE} and T^{SE} in the parallel and series

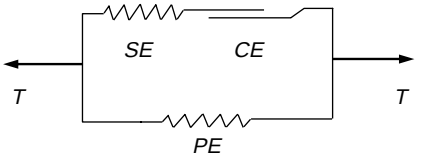

Figure 4. Hill's three-element muscle model: SE, series (elastic) element; CE, contractile element; PE, parallel (elastic) element; T, nominal stress.

elements, respectively,

$$T = T^{\mathrm{PE}} + T^{\mathrm{SE}}. \tag{5}$$

The stress T^{CE} in the contractile element satisfies:

$$T^{\mathrm{CE}} = T^{\mathrm{SE}}.$$

The unit vector, **n**, in the current direction of the muscle fibre is defined by

$$\mathbf{n} = \frac{\mathbf{FN}}{\lambda_{\mathrm{f}}}, \tag{6}$$

where **F** is the deformation gradient.

Because of the large deformations involved, the fibre stretch λ_{f} is decomposed into a multiplicative split of the contractile stretch followed by an elastic stretch:

$$\lambda_{\mathrm{f}} = \lambda^{\mathrm{CE}}\lambda^{\mathrm{SE}},$$

which corresponds to an additive Hencky strain decomposition.

The stresses T^{PE} and T^{SE} are highly non-linear functions of their elongations and essentially vanish in compression. They are strictly positive, i.e. the fibres can only work in tension. The stress T^{PE} is the product of the maximum tensile stress produced by the muscle at resting length, T_0^{M}, and a function of the stretch ratio:

$$T^{\mathrm{PE}}(\lambda_{\mathrm{f}}) = T_0^{\mathrm{M}} f^{\mathrm{PE}}(\lambda_{\mathrm{f}}), \tag{7}$$

where

$$f^{\mathrm{PE}}(\lambda_{\mathrm{f}}) = \begin{cases} 2aA\exp\left[a(\lambda_{\mathrm{f}}-1)^2\right](\lambda_{\mathrm{f}}-1), & \lambda_{\mathrm{f}} > 1 \\ 0, & \text{otherwise} \end{cases} \tag{8}$$

and a and A are constants. The stress T^{SE} is given by an analogous decomposition:

$$T^{\mathrm{SE}}(\lambda_{\mathrm{f}}, \lambda^{\mathrm{CE}}) = T_0^{\mathrm{M}} f^{\mathrm{SE}}(\lambda_{\mathrm{f}}, \lambda^{\mathrm{CE}}), \tag{9}$$

with

$$f^{\mathrm{SE}}\left(\lambda_{\mathrm{f}}, \lambda^{\mathrm{CE}}\right) = \frac{1}{10}\left\{\exp\left[100\left(\lambda_{\mathrm{f}} - \lambda^{\mathrm{CE}}\right)\right] - 1\right\}, \quad \lambda_{\mathrm{f}} \geq \lambda^{\mathrm{CE}}. \tag{10}$$

Both expressions (8) and (10) were obtained from the work carried out by Pandy et al. (1990).

The stress T^{CE} is given by the product of (1) a function of the contractile stretch, λ^{CE}, with maximum value at the muscle rest length, (2) a function of the strain rate of the contractile stretch, $\dot{\lambda}^{\mathrm{CE}}$, which, for contracting rates, corresponds to Hill's hyperbolic law and (3) an activation variable $\alpha \in [\alpha_{\min}, 1]$, with $\alpha_{\min} \geq 0$:

$$T^{\mathrm{CE}}(\lambda^{\mathrm{CE}}, \dot{\lambda}^{\mathrm{CE}}, \alpha) = T_0^M f_{\mathrm{L}}^{\mathrm{CE}}(\lambda^{\mathrm{CE}}) f_{\mathrm{V}}^{\mathrm{CE}}(\dot{\lambda}^{\mathrm{CE}})\alpha, \tag{11}$$

where

$$f_{\mathrm{L}}^{\mathrm{CE}}(\lambda^{\mathrm{CE}}) = 8\begin{cases} \lambda^{\mathrm{CE}^2} - \lambda^{\mathrm{CE}} + 0.25, & 0.5 \leq \lambda^{\mathrm{CE}} < 0.75 \\ -\lambda^{\mathrm{CE}^2} + 2\lambda^{\mathrm{CE}} - 0.875, & 0.75 \leq \lambda^{\mathrm{CE}} < 1.25 \\ \lambda^{\mathrm{CE}^2} - 3\lambda^{\mathrm{CE}} + 2.25, & 1.25 \leq \lambda^{\mathrm{CE}} < 1.5 \\ 0, & \text{otherwise} \end{cases}, \tag{12}$$

$$f_{\mathrm{V}}^{\mathrm{CE}}(\dot{\lambda}^{\mathrm{CE}}) = \begin{cases} (\dot{\lambda}^{\mathrm{CE}} + 10)\varepsilon, & \dot{\lambda}^{\mathrm{CE}} \leq -10\,\mathrm{s}^{-1} \\ -\frac{\arctan(-0.5\dot{\lambda}^{\mathrm{CE}})}{\arctan(5)} + 1, & -10\,\mathrm{s}^{-1} < \dot{\lambda}^{\mathrm{CE}} < 2\,\mathrm{s}^{-1} \\ (\dot{\lambda}^{\mathrm{CE}} - 2)\varepsilon + \frac{\pi}{4\arctan(5)} + 1, & \dot{\lambda}^{\mathrm{CE}} \geq 2\,\mathrm{s}^{-1} \end{cases} \tag{13}$$

and ε is a sufficiently small scalar introduced to avoid $f_{\mathrm{V}}^{\mathrm{CE}} = 0$ when $\dot{\lambda}^{\mathrm{CE}} \leq 10\,\mathrm{s}^{-1}$.

The time-dependent activation process involves the contractile element and is caused by neural excitation. At the macroscopic level, it is described by the first-order ordinary differential equation (ODE) proposed by Pandy et al. (1990):

$$\dot{\alpha}(u,t) = \frac{1}{\tau_{\mathrm{rise}}}(1 - \alpha(t))u(t) + \frac{1}{\tau_{\mathrm{fall}}}(\alpha_{\min} - \alpha(t))(1 - u(t)). \tag{14}$$

In Equation (14), τ_{rise} and τ_{fall} are the characteristic time constants for the activation and deactivation of the muscle and $\alpha_{\min}$ is the minimum value of activation. The function $u(t)$ ranges from 0 to 1, represents the neural excitation and is a part of the model's input data.

The approach followed in the present study assumes that the strain energy is stored isotropically in the material as well as in the direction of the muscle fibres and is given by

$$U = U(\mathbf{C}, \lambda^{\mathrm{CE}}) = \underbrace{U_{\mathrm{matrix}}(I_1^{\mathrm{C}})}_{U_{\mathrm{I}}} + \underbrace{U^{\mathrm{PE}}(\lambda_{\mathrm{f}}) + U^{\mathrm{SE}}\left(\lambda^{\mathrm{SE}}, \lambda^{\mathrm{CE}}\right)}_{U_{\mathrm{f}}}$$

where each of these energy terms originates the stress contributions (3) and (4), respectively.

The Cauchy stress tensor can also be written as:

$$\sigma = -p\boldsymbol{I} + 2\,\mathrm{dev}\left[\boldsymbol{F}\frac{\partial U}{\partial \boldsymbol{C}}\boldsymbol{F}^{\mathrm{T}}\right]. \tag{15}$$

As the diaphragm is very thin (3–5 mm), the above-mentioned 3D model is modified to agree with the thin shell theory (d'Aulignac et al. 2005; Martins et al. 2006, 2007).

In the case of a shell without shear deformation, the deformation gradient $\mathbf{F}$ is given by

$$\mathbf{F} = \begin{bmatrix} F_{11} & F_{12} & 0 \\ F_{21} & F_{22} & 0 \\ 0 & 0 & F_{33} \end{bmatrix} = \begin{bmatrix} \mathbf{F}_{\mathrm{p}} & 0 \\ 0 & F_{33} \end{bmatrix}.$$

As we assume perfect incompressibility, $J = \det \mathbf{F} = 1$, hence:

$$F_{33} = (\det \mathbf{F}_{\mathrm{p}})^{-1}.$$

Therefore, the Cauchy–Green strain tensors are given by

$$\mathbf{B} = \begin{bmatrix} \underbrace{\mathbf{F}_{\mathrm{p}}\mathbf{F}_{\mathrm{p}}^{\mathrm{T}}}_{\mathbf{B}_{\mathrm{p}}} & 0 \\ 0 & F_{33}^2 \end{bmatrix}, \quad \mathbf{C} = \begin{bmatrix} \underbrace{\mathbf{F}_{\mathrm{p}}^{\mathrm{T}}\mathbf{F}_{\mathrm{p}}}_{\boldsymbol{C}_{\mathrm{p}}} & 0 \\ 0 & F_{33}^2 \end{bmatrix}.$$

The first invariant can be calculated as:

$$\mathbf{I}_{\mathrm{I}}^{\mathrm{C}} = \mathrm{tr}(\mathbf{C}_{\mathrm{p}}) + C_{33}$$

The stretch ratio in the reference configuration can now be defined as

$$\lambda_{\mathrm{f}} = \sqrt{\mathbf{N}_{\mathrm{p}}^{\mathrm{T}}\mathbf{C}_{\mathrm{p}}\mathbf{N}_{\mathrm{p}}}$$

and the muscle fibre direction in the deformed configuration is given by

$$\mathbf{n}_{\mathrm{p}} = \frac{\mathbf{F}_{\mathrm{p}}\mathbf{N}_{\mathrm{p}}}{\lambda_{\mathrm{f}}},$$

where the subscript $\mathbf{p}$ in $\mathbf{N}_{\mathrm{p}}$ and $\mathbf{n}_{\mathrm{p}}$ concerns the in-plane (1,2) directions.

To obtain p, the conditions $\sigma_{i3} = 0$, $i \in \{1,2,3\}$ must be introduced, where the direction 3 of the orthonormal reference frame (1,2,3) follows the normal to the middle surface of the shell. The plane stress condition $\sigma_{33} = 0$ imposes a particular form for the pressure. From (15), we obtain:

$$p = \frac{1}{3}\left[2U_{\mathrm{I}}'(\mathrm{tr}[\mathbf{B}_{\mathrm{p}}] - 2C_{33}) + \lambda_{\mathrm{f}}U_{\mathrm{f}}'(\mathbf{n}_{\mathrm{p}} \otimes \mathbf{n}_{\mathrm{p}})\right], \qquad (16)$$

with $U_{\mathrm{I}}' = \partial U_{\mathrm{I}}/\partial I_{\mathrm{I}}^{\mathrm{C}}$ and $U_{\mathrm{f}}' = \partial U_{\mathrm{f}}/\partial \lambda_f$.

Therefore, the Cauchy stress in the plane is given by

$$\sigma_{\mathrm{p}} = 2U_{\mathrm{I}}'(\mathbf{B}_{\mathrm{p}} - B_{33}\mathbf{I}_{\mathrm{p}}) + \lambda_{\mathrm{f}}U_{\mathrm{f}}'(\mathbf{n}_{\mathrm{p}} \otimes \mathbf{n}_{\mathrm{p}}). \qquad (17)$$

The simulations performed are based on the constitutive Equation (17).

Owing to the strict monotonicity and invertibility in $\Re$ of $f_{\mathrm{V}}^{\mathrm{CE}}$, the time rate of change of the internal variable λ^{CE} is governed by the first-order ODE:

$$\dot{\lambda}^{\mathrm{CE}}\left(\lambda_{\mathrm{f}}, \lambda^{\mathrm{CE}}, \alpha, \dot{\lambda}_{\mathrm{f}}, u\right) = f_{\mathrm{V}}^{\mathrm{CE}^{-1}}\left(\lambda_{\mathrm{f}}, \lambda^{\mathrm{CE}}, \alpha, \dot{\lambda}_{\mathrm{f}}, u\right). \qquad (18)$$

To solve the two ODEs (14) and (18), the backward-Euler scheme is used. The tangent modulus consists of the derivative of σ_{p} with respect to the strain rate.

4. Application to the diaphragmatic floor

4.1 Input data

The diaphragm was modelled using triangular S3 shell elements and the muscle behaviour was incorporated in ABAQUS by implementing a UMAT subroutine.

The tendinous part of the diaphragm was considered linear, elastic and isotropic with values for Young's modulus and Poisson's coefficient of 33 MPa and 0.33, respectively (Behr et al. 2006). The material parameters used for the muscle were chosen from Humphrey and Yin (1987): $b = 23.46$; $c = 3.79517355 \times 10^{-4}$ MPa; $A = 8.73206 \times 10^{-4}$; $a = 12.43$ and $T_0^{\mathrm{M}} = 6.5586872 \times 10^{-1}$ MPa. The values for the constants in Equation (14) were $\tau_{\mathrm{rise}} = 20 \times 10^{-3}$ s; $\tau_{\mathrm{fall}} = 20 \times 10^{-3}$ s and $\alpha_{\mathrm{min}} = 0.01$. The value for the parameter ε in definition (13) was $\varepsilon = 1 \times 10^{-4}$.

A constant excitation with value u_{max} was applied during inspiration for a period of time of 2 s. After this period of time, the neural excitation was set to zero during the remaining 3 s of the complete respiratory cycle.

The pressure profile in the surface of the diaphragm was difficult to obtain. Instead, the pressure between the inside and outside of the diaphragmatic surfaces, called the transdiaphragmatic pressure (Pdi), was used. The Pdi during normal and quiet breathing had a value of about 5 cm H_2O (490.333 MPa; Tobin et al. 2002). The pressure profile along the surface was not uniform. For simplification, only two regions (apposition and diaphragmatic regions) were considered (Figure 5), and a constant pressure was applied in their outer surfaces. During inspiration, pressures of 4.9033×10^{-4} MPa and -4.9033×10^{-4} MPa were applied to the diaphragmatic and apposition zones, respectively. During expiration, opposite pressures were applied to the same regions.

In the present study, all nodes at the inferior borders of the model were considered fixed in displacement. The vena cava and oesophageal apertures as well as the aortic opening were kept fixed along the sagittal and coronal axes, but the axial displacement of their borders was kept free. The boundary was free to rotate with the exception of border regions, A and L, of the inferior border (see Figure 6). In Region A (anterior), the nodes could not

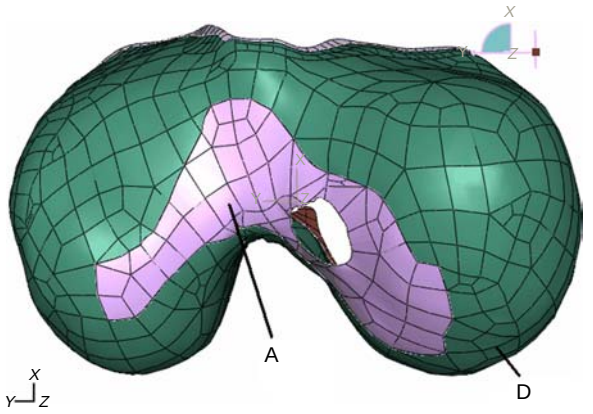

Figure 5. Apposition (A) and diaphragmatic (D) regions in the geometric model.

rotate about the *x*-axis, and in Region L (lateral left and right), the nodes could not rotate about the *y*-axis. These boundary conditions did not change with time during the respiratory cycle.

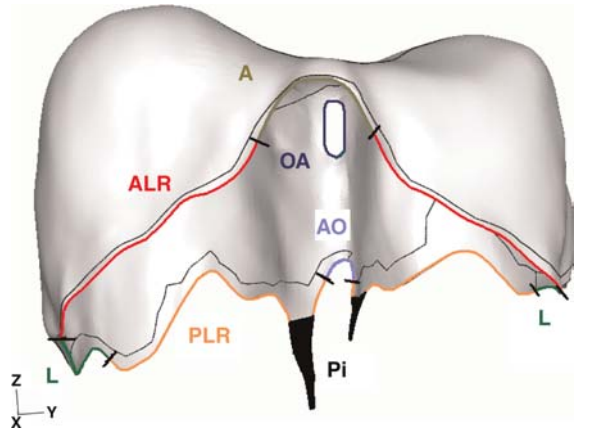

Figure 6. Boundary Conditions: A-anterior, ALR-anterior left/right, PLR-posterior left/right, L-lateral, OA-oesophageal aperture, AO-aortic opening and Pi-pillars.

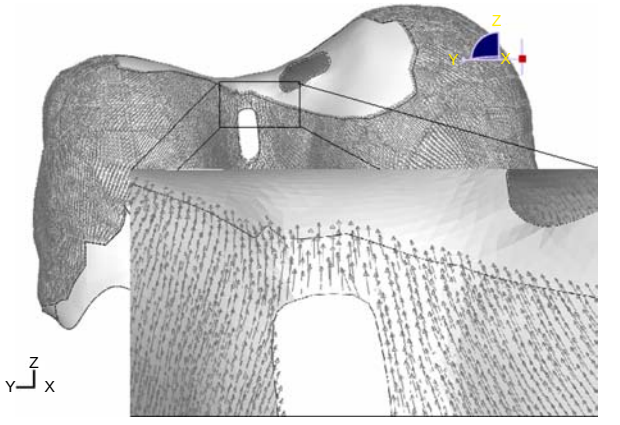

Figure 7. Radial pattern of the direction of the fibres.

The initial conditions used in (14) and (18) were $\alpha(0) = 0.01$, $\lambda_f(0) = 1.0$ and $\lambda^{CE}(0) = 0.982082$.

The initial directions of the muscle fibres were determined according to a radial pattern (see Figure 7). In fact, the direction of the majority of the fibres was radial, starting at the phrenic centre and ending at the inferior borders of the diaphragm (for more details, see Santos 2009).

4.2 *Numerical results*

First FE simulations of the diaphragm were performed considering different values for the threshold, u_{max}, in the neural excitation u. The results obtained for the tidal volume (TV) as well as for the maximum axial displacement (MAD) of the diaphragm are shown in Figure 8. The values given in the literature (Segars et al. 2001; Gaillard 2003) and the results obtained suggest that the best interval for u_{max}, to characterise the excitation in a normal quiet breathing, is between 20 and 30%.

The simulation of a normal quiet breathing was performed during a period of 5 s and with $u_{max} = 0.3$. The evolution of the volume and MAD of the top of the diaphragm is shown in Figure 9. The volume of the diaphragm under analysis was calculated as the difference between two volumes: one obtained from its initial shape and the other from its deformed configuration in a later phase of respiration. The TV was approximately 564 cm^3, while the MAD was about 10.6 mm.

During inspiration, the diaphragm contracted, the domes of the diaphragm descended and its apposition as well as its anterior and posterior zones shrunk. The decrease in the height of the domes was larger in the right dome, where the MAD was obtained. The horizontal displacements of the lateral sides of the diaphragm were two to three times smaller than the axial displacement of the domes. In fact, the latter was approximately two to three times greater than the former. The posterior zone of the diaphragm demonstrated a smaller contraction when compared with the displacement of the apposition and anterior parts of the diaphragm. During expiration, the diaphragm demonstrated a quasi-symmetric behaviour relatively to the inspiration. The domes ascended and the lateral sides moved to the outside due to the relaxation of the muscle. Both the volume and MAD evolutions presented four different regions during the respiratory cycle. During inspiration, all the variations in volume and displacement took place approximately at the first second of the analysis. Likewise, during expiration, all the variation occurred approximately during the first one and a half seconds. During these periods of time, the evolution showed a quasi-exponential behaviour. At the remaining periods of time, the variation was inexistent.

Two pathological cases were analysed: a diaphragmatic dysfunction due to an ALS disease and a complete right phrenic nerve lesion (RPNL). The difference between these two cases and the normal case was the inactivation of the

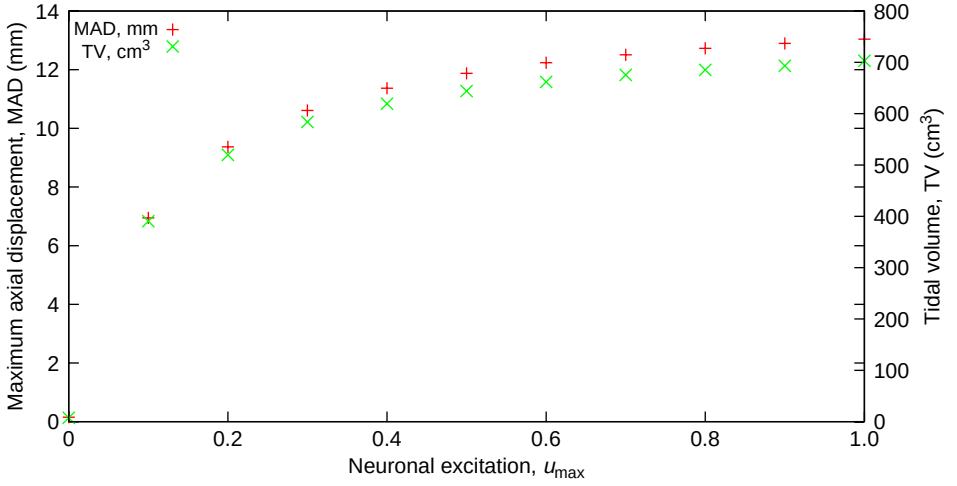

Figure 8. MAD (+) and TV (×) at the end of the inspiration as a function of u_{max}.

relevant fibres in the pathological diaphragms. In the normal case, all the fibres may be activated. In the ALS case, the inactivation demonstrated a random pattern with about half of the fibres of the muscle with zero excitation. In the RPNL case, all the fibres in the right side of the muscle were inactivated. Figure 9 also shows the variations of the volume and MAD of the diaphragm for these two pathological conditions. The evolutions of volume and displacement in both the cases were similar and analogous to the corresponding evolutions in the normal case. In the ALS disease, during inspiration, both the domes of the diaphragm descended axially and the lateral parts of the diaphragm shrunk as a result of the contraction of the healthy fibres of the muscle. However, these movements were smaller than those in the normal diaphragm. In the RPNL simulation, during inspiration, only the left side of the diaphragm contracted, and hence, suffered a larger deflection than the right side. The paralysed right hemidiaphragm did not shrink as much as the left side. Furthermore, the domes descended less than the healthy case. During expiration, the movement of the diaphragm in both the pathological cases was symmetric relatively to that during inspiration, like that during normal breathing.

In the pathological cases, both TV and MAD decreased significantly. In the ALS case, the TV was approximately 306 cm^3 and the maximum descent of the domes was about

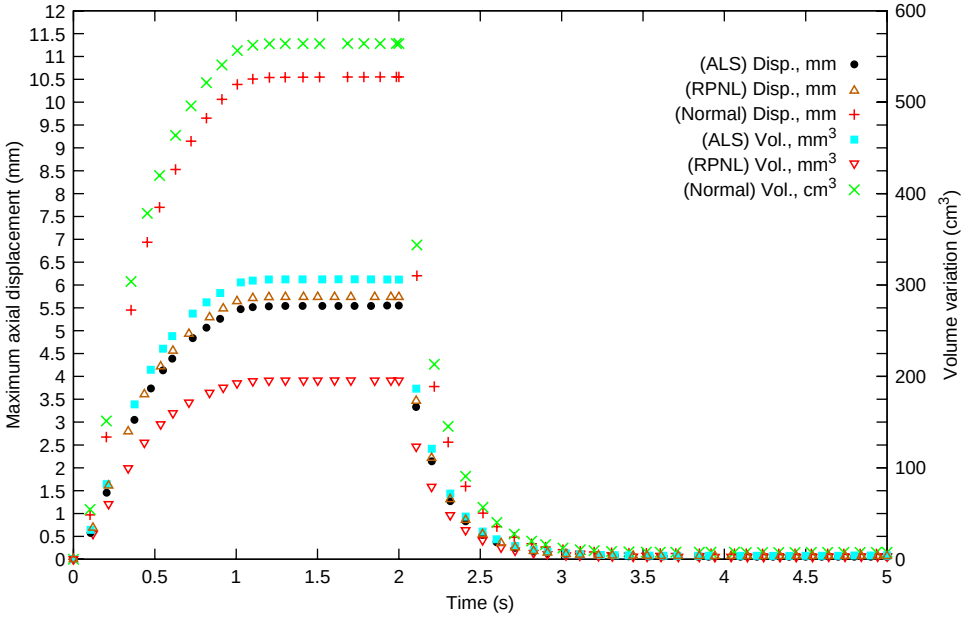

Figure 9. Mad and volume variations in the normal and two pathological cases for $u_{max} = 0.3$.

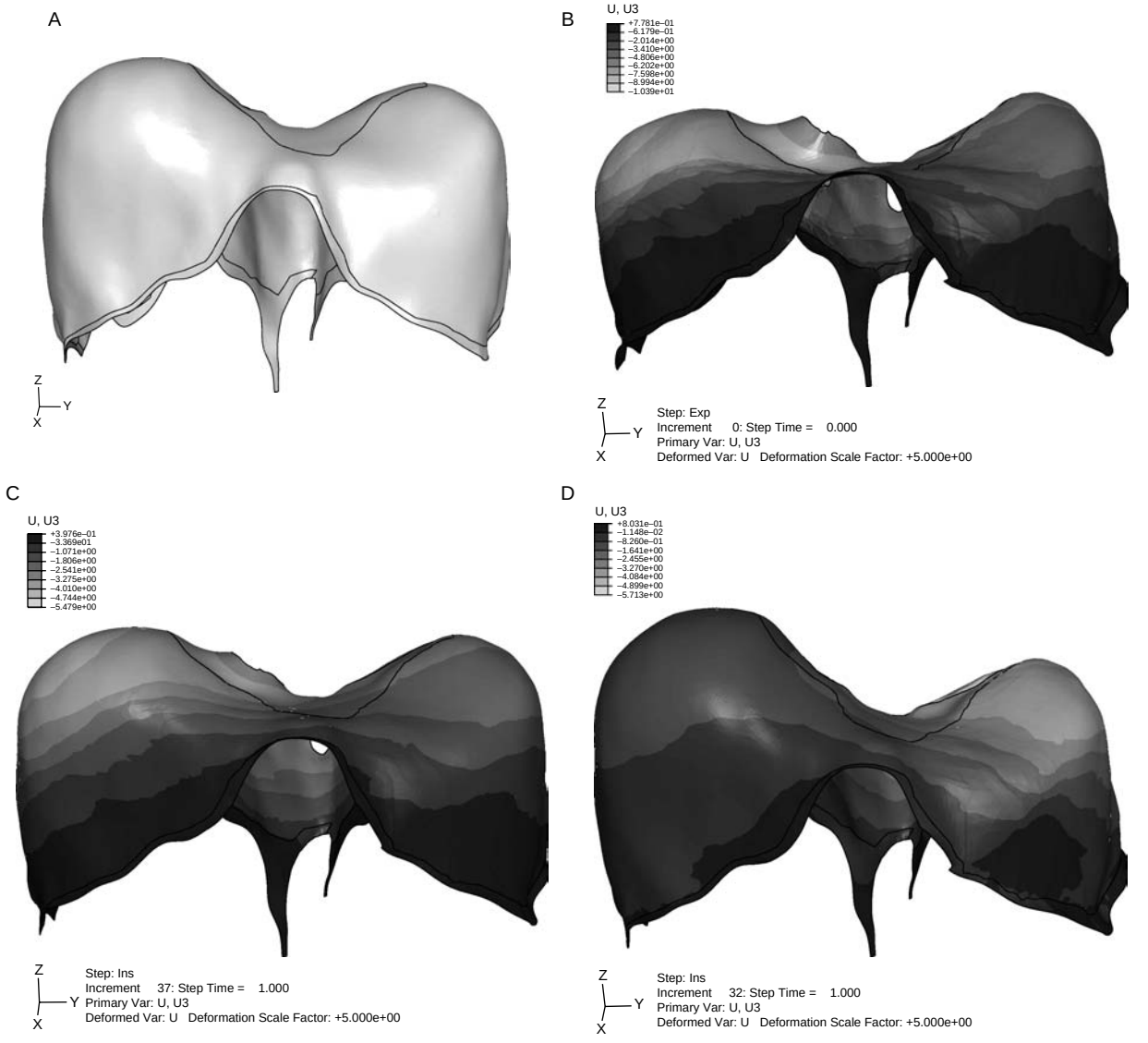

Figure 10. Vertical displacement of the diaphragm (U_3): (A) before inspiration and at the end of inspiration, (B) in the normal case, (C) in the ALS case and (D) in the RPNL case.

5.55 mm (54.3 and 52.6% of the value of the normal case, respectively). In the RPNL case, the TV was about 196 cm^3 and the descent was approximately 5.74 mm (34.8 and 54.4% of the value of the normal case, respectively). The MAD occurred in the right dome in the ALS case as in the normal case, but its location changed to the left dome in the RPNL case due to the inactivation of the right hemidiaphragm.

Figure 10 illustrates the movement of the diaphragm at the end of inspiration in all the three cases. Animations of this movement as well as the maximum principal stresses during the respiratory cycle can be found in http://www.civil.ist.utl.pt/mpato.

5. Conclusions

During normal breathing (as well as in the pathological cases), periods of time with no variation in volume and MAD occur. This suggests that during a normal quiet breathing, the time duration of the respiratory cycle is probably smaller ($\sim$3 s) because the diaphragmatic muscle during inspiration and the expiratory muscles during expiration require a smaller period of time to contract. However, the periods of time when there is no variation may represent periods for gas exchange and muscle relaxation.

In both the pathological cases, the behaviour and performance of the diaphragm presented differences during respiration, although in the RPNL case, the differences were

more significant. In both the cases, the TV was smaller than in the normal breathing case as expected. However, the TV of the ALS case was approximately 110 cm^3 greater than that in the RPNL case. It is known that the effect of the inactivation of the fibres in one of the hemidiaphragms is not significant in the performance of quiet breathing. This suggests that in the RPNL case, there is an active compensation from the other inspiratory muscles or even from a reinforcement of healthy fibres, which does not occur in the ALS cases. As a result, a value for u_{max} greater than 0.3 should be considered in this case.

The diaphragm has a movement relative to the body as a consequence of the movement of the other inspiratory muscles and ribs. As a future development, analyses should consider the borders of the diaphragm to displace during respiration. The values of the displacement of the inferior borders of the diaphragm may be determined from the medical imaging taken during quiet breathing or obtained from the literature.

Acknowledgements

The authors gratefully acknowledge the Fundação para a Ciência e a Tecnologia for the support granted in the context of POCI 2010 and for the PhD grant SFRH/BD/47750/2008.

References

Ackerman M. 1998. The visible human project. Proceedings of the IEEE 86: 504–511.

Behr M, Thollon L, Arnoux P, Serre T, Berdah S, Baque P, Brunet C. 2006. 3D reconstruction of the diaphragm for virtual traumatology. Surg Radiol Anat. 28:235–240.

d'Aulignac D, Martins J, Pires E, Mascarenhas T, Natal Jorge R. 2005. A shell finite element model of the pelvic floor muscles. Comput Methods Biomech Biomed Eng. 8: 339–347.

de Mamede C. 2002. Neurophysiology as an early measure of disease progression. Clin Neurophysiol. 113:S1–S4.

de Troyer A, Leeper J, McKenzie D, Gandevia S. 1997. Neural drive to the diaphragm in patients with severe COPD. Am J Respir Crit Care Med. 155:1335–1340.

Fung Y. 1993. Skeletal muscle. In: Biomechanics mechanical properties of living tissues, 2nd ed. Chapter 2. New York: Springer-Verlag. p. 392–425.

Gaillard L. 2003. Modèle fonctionnel du diaphragme pour l' acquisition et le diagnostic en imagerie médicale [master's thesis]. [La Tronche (France)]: Université Joseph Fourier.

Grieve A, Armstrong C. 1988. Compressive properties of soft tissues. In: Biomechanics XI-A, International series on Biomechanics. Amsterdam: Free University Press, Vol. 53, p. 1–536.

Harrison G. 2005. The anatomy and physiology of the diaphragm. In: Upper gastrointestinal surgery. London (UK): Springer. p. 45–58.

Hill A. 1938. The heat of shortening and the dynamic constants of muscle. Proc Roy Soc London. B129:136–195.

Humphrey J, Yin F. 1987. On constitutive relations and finite deformations of passive cardiac tissue: I. A pseudostrain-energy function. ASME J Biomech Eng. 109:298–304.

Laroche C, Mier A, Moxham J, Green M. 1998. Diaphragm strength in patients with recent hemidiaphragm paralysis. Thorax. 43:170–174.

Lopes D, Martins J, Pires E. 2008. Three-dimensional reconstruction of biomechanical structures for finite element analysis. In: *st Workshop on Computational Engineering: Fluid Dynamics, Portugal-UT Austin CFD, Instituto Superior Técnico*.

Martins J, Pato M, Pires E. 2006. A finite element model of skeletal muscles. Virtual Phys Prototyping. 1:159–170.

Martins J, Pato M, Pires E, Natal Jorge R, Parente M, Mascarenhas T. 2007. Finite element studies of the deformation of the pelvic floor. Ann NY Acad Sci. 1101: 316–334.

Pandy M, Zajac F, Sim E, Levine W. 1990. An optimal control model for maximum-height human jumping. J Biomech. 23:1185–1198.

Ratnovsky A, Elad D, Halpern P. 2008. Mechanics of respiratory muscles. Respir Physiol Neurobiol. 163:82–89.

Santos N. 2009. Preliminary biomechanical studies on the diaphragmatic function in control and patients with loss of motor units [master's thesis]. [Lisbon (Portugal)]: Instituto Superior Técnico.

Segars W, Lalush D, Tsui B. 2001. Modeling respiratory mechanics in the mcat and spline-based mcat phantoms. IEEE Trans Nucl Sci. 48:89–97.

Spitzer V, Ackerman M, Scherzinger A, Whitlock D. 1996. The visible human male: A technical report. Journal of the American Medical Informatics Association. 3:118–130.

Tobin M, Brochard L, Rossi A. 2002. Assessment of respiratory muscle function in the intensive care unit. Am J Respir Crit Care Med. 166:610–623.